GEOLOGY | THE GEOLOGICAL SOCIETY OF AMERICA®

https://doi.org/10.1130/G51127.1

Manuscript received 30 January 2023
Revised manuscript received 11 April 2023
Manuscript accepted 17 April 2023

Three-dimensional mineral dendrites reveal a nonclassical crystallization pathway

Zhaoliang Hou[1], Dawid Woś[2], Cornelius Tschegg[3], Anna Rogowitz[1,4], A. Hugh N. Rice[1], Lutz Nasdala[5], Florian Fusseis[6], Piotr Szymczak[2,*], and Bernhard Grasemann[1,*]
[1]Department of Geology, University of Vienna, Vienna 1090, Austria
[2]Institute of Theoretical Physics, Faculty of Physics, University of Warsaw, Warsaw 02-093, Poland
[3]Glock Health, Science and Research GmbH, Deutsch-Wagram 2232, Austria
[4]Institute for Earth Sciences, University of Graz, Graz 8010, Austria
[5]Institute of Mineralogy and Crystallography, University of Vienna, Vienna 1090, Austria
[6]School of Geosciences, University of Edinburgh, Edinburgh EH9 3FE, UK

ABSTRACT

Manganese (Mn) dendrites are a common type of mineral dendrite that typically forms two-dimensional structures on rock surfaces. Three-dimensional (3-D) Mn dendrites in rocks have rarely been reported, and so their growth implications have largely escaped attention. Here, we combined high-resolution X-ray and electron-based data with numerical modeling to give the first detailed description of natural 3-D Mn dendrites (in clinoptilolite tuffs) and elucidate their growth dynamics. Our data show that 3-D dendrite growth occurred by accretion of Mn-oxide nanoparticles formed when Mn-bearing fluids mixed with oxygenated pore water. The geometry of the resulting structures is sensitive to ion concentrations, the volume of infiltrating fluid, and the number of fluid pulses; thus, 3-D dendrites record the hydrogeochemical rock history.

INTRODUCTION

In contrast to metallic/crystalline dendrites formed by solidification of supercooled melts (Trivedi and Kurz, 1994), mineral dendrites are a fingerprint of unstable aqueous growth processes, driven by an interplay between fluid motion and chemical concentration gradients (Chopard et al., 1991; García-Ruiz et al., 1994; Meakin and Jamtveit, 2010). Mn mineral dendrites form by oxidative precipitation of Mn and typically grow as planar two-dimensional structures on rock surfaces (Chopard et al., 1991; García-Ruiz et al., 1994). Although three-dimensional (3-D) Mn dendrites have been reported (Van Straaten, 1978), their growth processes remain enigmatic. The 3-D gold/electrum dendrites from epithermal conditions are better studied (Saunders, 2022; Monecke et al., 2023).

We studied natural 3-D Mn dendrites using combined microscale analyses and numerical modeling (Supplemental Material[1]). The data show that our dendrites encode the hydrogeochemical history of the rock, including the number and relative volumes of infiltrating Mn-rich fluid pulses. We also show that dendrite growth proceeded through the formation, diffusion, and attachment of Mn-oxide nanoparticles, a nonclassical crystallization pathway that is increasingly being recognized as an important crystal growth mechanism (De Yoreo et al., 2015; Hochella et al., 2019).

SAMPLE BACKGROUND

The Mn dendrites documented here occur in clinoptilolite tuffs at Nižný Hrabovec, Slovak Republic (Fig. 1A; Fig. S2A). The chemically and mineralogically homogeneous 16.3–15 Ma tuff formed from pure rhyolitic volcanic ash that was zeolitized at 44–84 °C (Tschegg et al., 2019). The tuff has abundant inter- and intragranular pores, allowing fluid-borne metals to diffuse into clinoptilolite grains and be loosely sorbed into the crystal lattice (Tschegg et al., 2020).

Dendrites are formed by different mineral associations, with their composition being neither singular nor universal. Our dendrites, comprising amorphous Mn-oxides (Fig. S3), grew adjacent and perpendicular to Mn-coated fractures in the tuffs. To simplify descriptions, we define a local reference frame where the fractures are horizontal and "below," and dendrites grow "upward."

MORPHOLOGY OF 3-D DENDRITES

X-ray microtomography revealed a 3-D dendrite "forest" in the clinoptilolite tuff (Fig. 1B; Movie S1). Overall, the <15-mm-high forest had a volume fraction of ~23% (107 mm^3 in 467 mm^3 rock), with dendrite abundance decreasing in a power-law scaling with forest height (Fig. S2C). All dendrites had a core surrounded by an ~17-µm-thick outer rim (Fig. 1C). The forest base, which was located adjacent to the fracture surface, was composed of a continuous layer of dendrite core material, with only small, irregular holes remaining (Fig. 1D), connecting the fracture void to the clinoptilolite tuff. The dendrites had a straight, subcircular primary trunk with a botryoidal surface morphology and a scallop-like top (Fig. 1B). Short conical to cylindrical branches made the dendrite shape increasingly bulky upward, as reflected in a slight increase in the forest's 3-D fractal dimension, from ~2.70 to 2.80 (Fig. S2D).

Digital microscope data on polished sections oriented normal to fractures characterized the

---

Zhaoliang Hou https://orcid.org/0000-0003-4937-2940
*corresponding authors: Szymczak: piotrek@fuw.edu.pl; Grasemann: bernhard.grasemann@univie.ac.at

[1] Supplemental Material. Supplemental methods, Figures S1–S4, and Movies S1 and S2. Please visit https://doi.org/10.1130/GEOL.S.22661659 to access the supplemental material, and contact editing@geosociety.org with any questions.

CITATION: Hou, Z., et al., 2023, Three-dimensional mineral dendrites reveal a nonclassical crystallization pathway: Geology, v. 51, p. 626–630, https://doi.org/10.1130/G51127.1

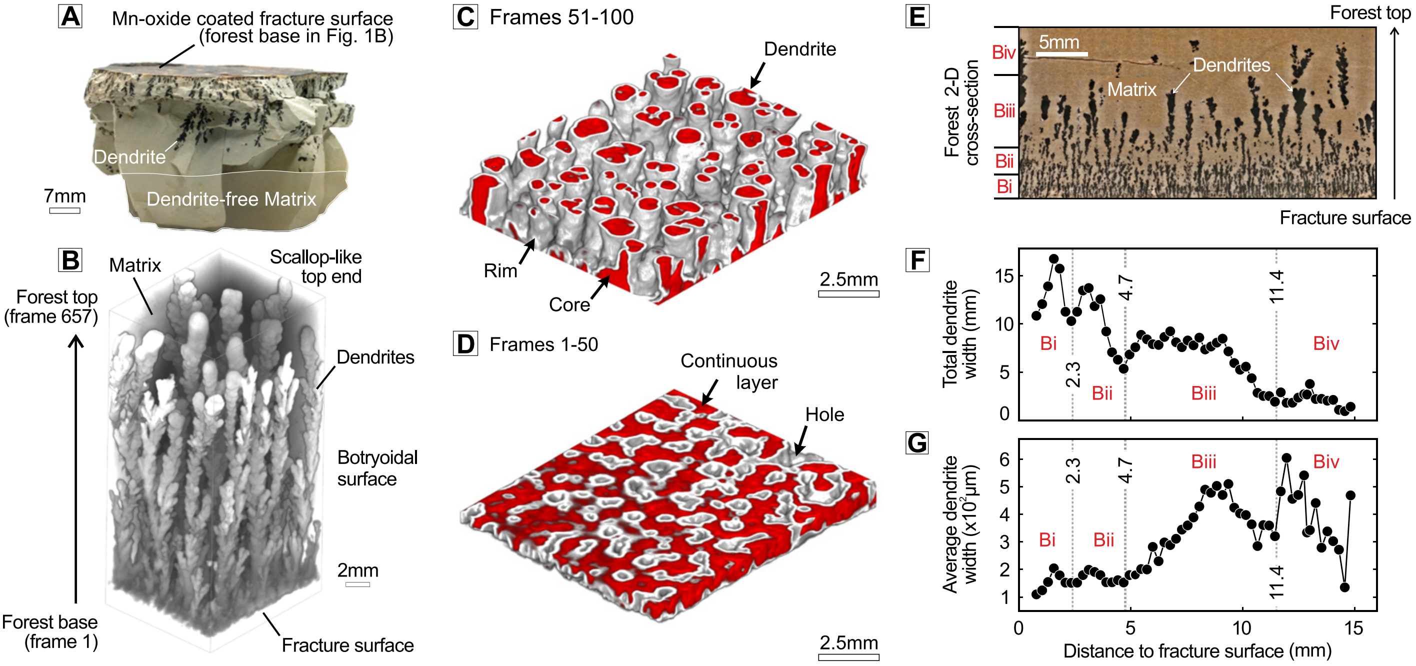

Figure 1. Three-dimensional morphology of dendrite forest. (A) Mn dendrites in hand specimen. (B) Micro–computed tomography (µCT) image of dendrite forest in clinoptilolite tuff. (C–D) Visualized dendrite trunks (C) and forest base (D) from part B. (E) Digital microscope mosaic of polished sample. (F–G) Variations in combined dendrite width (F) and average width (G) with distance from fracture surface.

forest geometry (Fig. 1E). Four non-overlapping conical branch groups formed during dendrite growth (Bi–Biv), shown by fluctuations in the combined dendrite width (Fig. 1F) and the average individual dendrite width (Fig. 1G): Bi was at 0–2.3 mm from the forest base, Bii at 2.3–4.7 mm, Biii at 4.7–11.4 mm, and Biv at >11.4 mm. Total dendrite width decreased from ~16.1 to 0.9 mm (Fig. 1F), and average dendrite width increased from ~154 µm to 383 µm from Bi to Biv (Fig. 1G). Dendrite volume fractions decreased from ~40% to 0% (Fig. S4).

Individual dendrites all had a trunk domain at the base and a branching domain farther up (Fig. 2A). Branching domains widened toward dendrite tops, especially Biii and Biv, within which the dendrites developed a concentric architecture consisting of alternating layers of core and rim material (Figs. 2A and 2B). All dendrites in a sample had the same number of internal layers at a given distance from the fracture surface (Fig. 2B).

CHEMISTRY AND MICROSTRUCTURES

Scanning electron microscope (SEM) observations of thin sections showed that dendrite growth reduced the original porosity from ~17% in the matrix to ~1%–4% in the internal rims, and 0% in the cores (Figs. 2C–2E and 2C′–2E′).

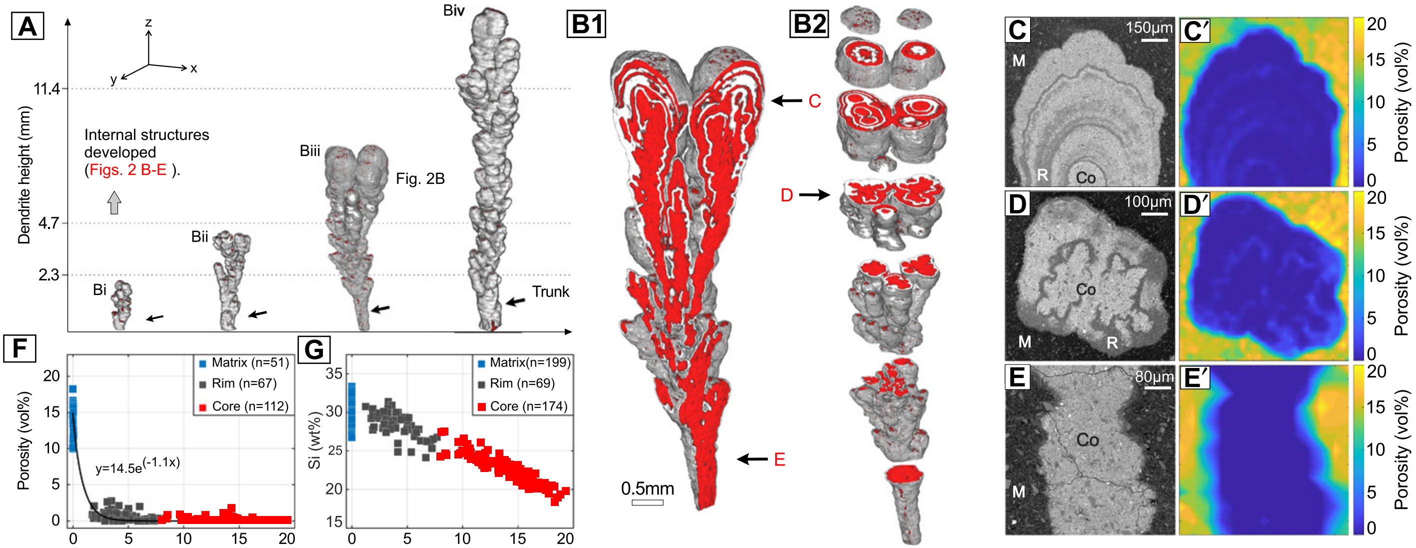

(C-E: Co: Core; R: Rim; M: Matrix)

Figure 2. Structures of individual dendrites. (A) Visualized dendrites showing morphologies from Bi to Biv. (B) Dendrite longitudinal (B1) and horizontal sections (B2). (C–E) Scanning electron microscope–backscattered electron (SEM-BSE) mosaics showing structure of dendrite top (C), middle (D), and base (E). (C′–E′) Corresponding porosity maps. (F) Variation of Mn concentration with porosity. (G) Variation of Mn and Si from matrix to core.

The outer rims adjacent to the matrix had a steep porosity gradient, from 17% to 4% (Figs. 2C′–2E′). Electron probe micro-analyzer (EPMA) line scans across dendrites and into the matrix indicated that Mn concentrations were linked to dendrite core-rim architecture (Figs. 2F and 2G). Increasing Mn concentrations from matrix to core were accompanied by an exponential drop in porosity (Fig. 2F) and a linear decrease in silicon concentration (Fig. 2G). No Mn was present in the matrix (Fig. 2G). Rim Mn concentrations varied between 1.3 and 7.7 wt%, and core Mn concentrations varied between 8.0 and 19.3 wt%. In contrast, the silicon decreased from the matrix (6.7 wt% variation) to the cores (~3.5 wt% variation at a given Mn concentration; Fig. 2G). Silicon was not mobile, but the addition of Mn oxides reduced its proportion.

High-resolution SEM images showed subangular to rounded, several-nanometer- to 1-µm-sized (average 380 nm) Mn-oxide nanoparticles in dendrites (Figs. 3A and 3B) but not the matrix (Fig. 3C). These particles formed larger aggregates, rather than being individually distributed and randomly attached to the rock (Fig. 3B). Although the nanoparticle aggregates looked the same in cores and rims, they occurred in different pore contexts. In the cores, backscattered electron (BSE) images showed that Mn oxide completely filled both inter- and intragranular pores and was also sorbed into the clinoptilolite crystal lattice (confirmed by EPMA). Only the centers of large clinoptilolite grains (>13 µm size) were free of Mn oxides, although infiltration into marginal intragranular pores occurred (Fig. 3D). In the rims, intergranular pores were filled by Mn oxide, but intragranular pores were unaffected (Fig. 3E). No Mn oxide was observed in the matrix (Fig. 3F).

DISCUSSION AND CONCLUDING REMARKS

Dendrite Growth Processes

Since the tuff was initially chemically and mineralogically homogeneous, and without heavy metals, a pulse of Mn-rich fluid must have infiltrated the rock through preexisting fractures. We hypothesize that the fluid pushed an oxygenated matrix pore fluid away from the fracture and mixed with it, generating an oversaturated Mn-oxide solution (Fig. 4A, b0). Laboratory studies on Mn oxide (Li et al., 2014; Huang et al., 2015) have confirmed that such conditions promote the initial growth of Mn-oxide nanoparticles. This is consistent with our observation of Mn-oxide particles on dendrite surfaces (Figs. 3A and 3B). We thus propose that Mn-oxide particles formed in the pore fluid, diffused through the rock matrix, and became attached to the Mn-oxide–coated fracture (Fig. 4A, b1), initiating dendrite growth. Such a nonstandard crystallization pathway, via particle attachment, is increasingly being recognized as an important and widespread type of crystal growth (Ivanov et al., 2014; De Yoreo et al., 2015; Hochella et al., 2019).

Since the fractal dimension of the dendrites increases with increasing length scales, the dendrite forest is not completely scale-free. This is likely due to the relatively high Mn particle concentration prevailing during dendrite growth, implying the existence of finite concentration effects. This leads to the formation of a diffusive boundary layer and hence introduces an additional length scale into the system (Voss, 1984;

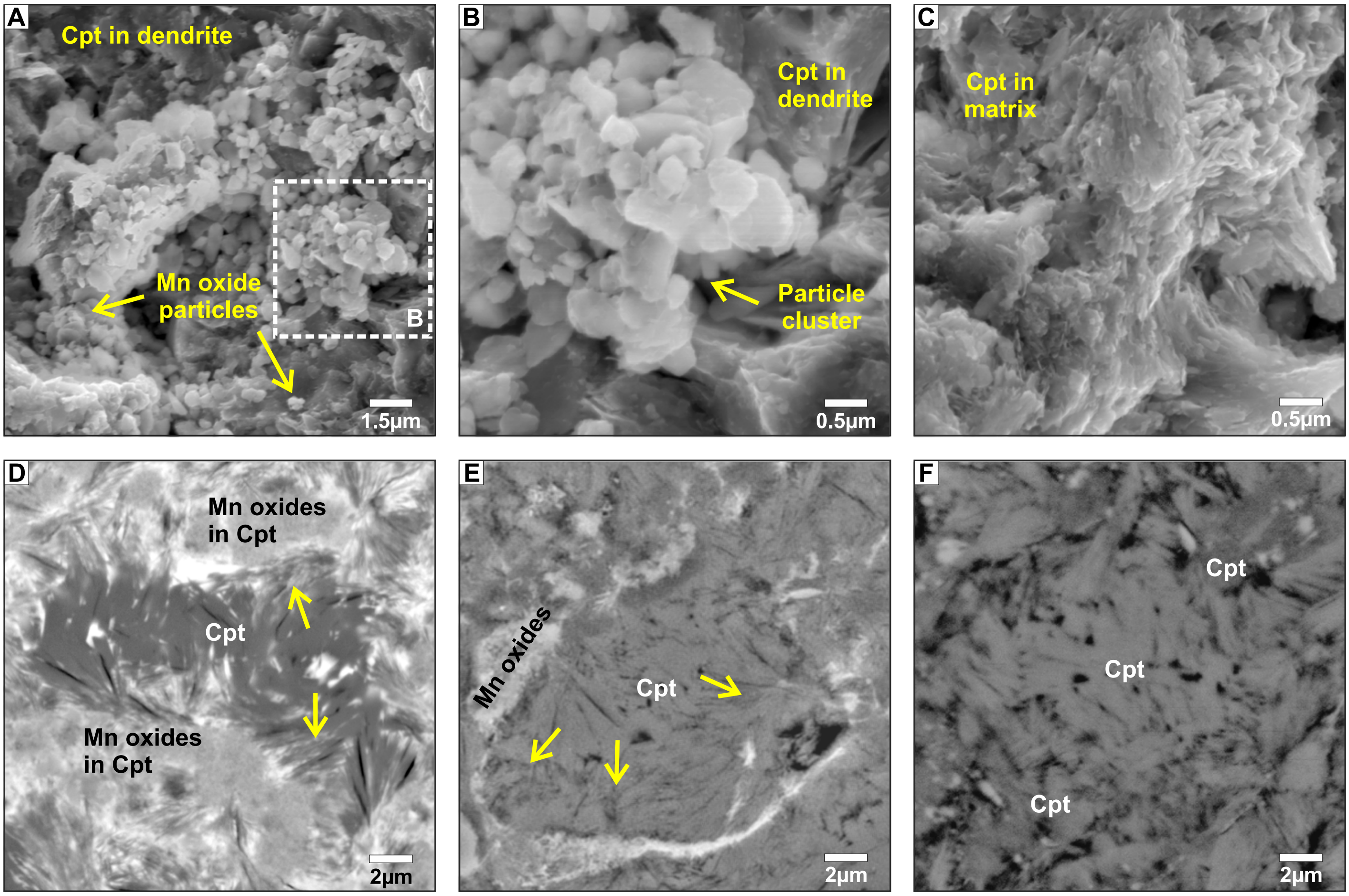

Figure 3. Dendrite internal structure. (A–C) Scanning electron microscope–secondary electron (SEM-SE) images showing structure of Mn-oxide particles in dendrites (A–B) and none in matrix (C). (D–E) Scanning electron microscope–backscattered electron (SEM-BSE) images showing details of Mn-oxide concentrations from dendrite cores (D) and rims (E) to matrix (F). Arrows point to intragranular porosity (D, E). No Mn oxide is observed in matrix (F). Cpt—clinoptilolite.

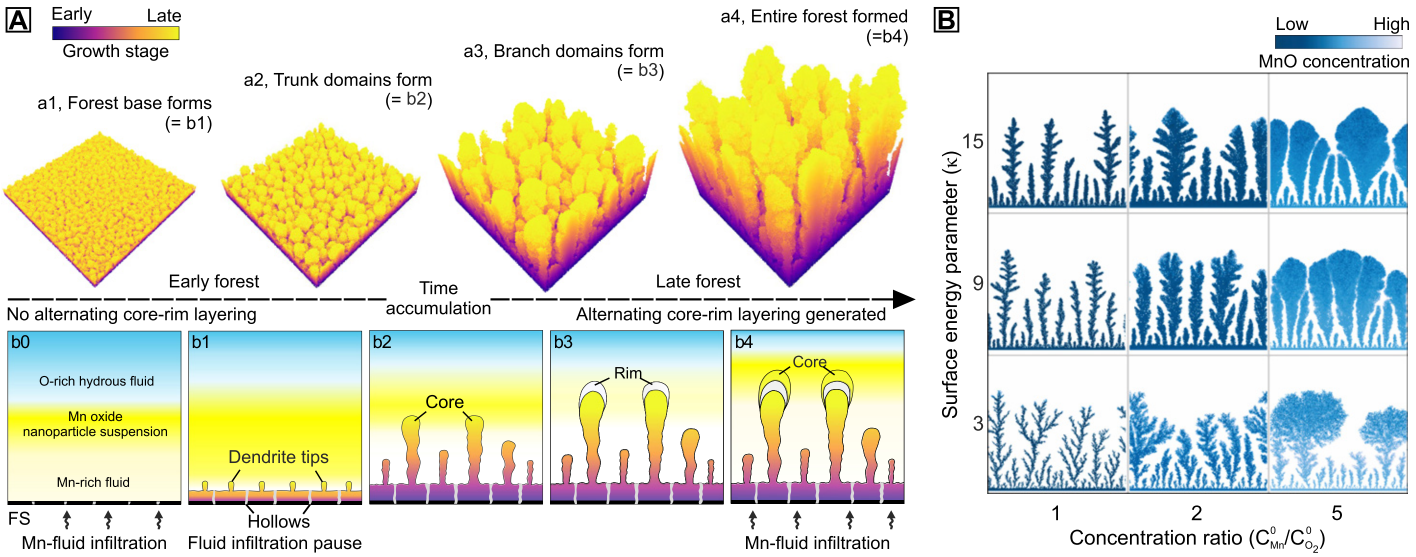

Figure 4. Dendrite growth models. (A) Numerical (a1–a4) and conceptual (b0–b4) models. Background color gradients in b0–b4 represent particle concentrations; darker colors indicate higher concentrations. (B) Morphological diagram of modeled dendrites. FS—fracture surface.

Meakin and Deutch, 1984; Fowler et al., 1989). Variations in dendrite abundance and width (Bi to Biv) demonstrate that dendrites competed for nanoparticles. Such competitive dynamics lead to a power-law distribution of dendrite lengths, $N(L) \sim L^{-\alpha}$, where $N(L)$ denotes the number of dendrites longer than L (Krug, 1997). In our case, $\alpha \approx 1.25$ (Fig. S2C), in line with the scaling reported for similar fingered growth systems, such as dissolution channels (Szymczak and Ladd, 2006).

With ongoing dendrite growth, the Mn-oxide nanoparticle concentration in the pore fluid decreased continuously (Fig. 4A, b2). At a certain concentration, the chemical potential gradient driving nanoparticle diffusion was insufficient to overcome the energy barrier for diffusion into intragranular pore space, so the clinoptilolite grains remained Mn-oxide-free, and precipitation proceeded in intergranular pores only, sealing off the intragranular porosity and forming rim material (Fig. 4A, b3).

A unique feature of our dendrites is their banding, with alternating layers of core and rim material. Dendrites in a thin section showed the same number of core-rim layers at any given distance from the fracture, implying that the banding was due to overall changes in nanoparticle concentration in the pore fluid, rather than to local precipitation dynamics. The occurrence of rims only in the upper part of longer dendrites strongly suggests that growth proceeded by accretion of particles diffusing from above, in discrete pulses.

Each pulse of Mn-rich fluids pushed the interface with the oxygenated matrix pore fluid beyond the dendrites, creating a new batch of nanoparticles. By diffusion, these particles reached existing dendrites first, especially longer ones, and attached preferentially to their tips, overgrowing the existing rims and forming a new core layer (Fig. 4A, b4) and then, after nanoparticle depletion, a rim. When no further fluid pulses occurred, dendrite growth ceased.

The core-rim succession cannot be explained by the viscous fingering model for dendrite growth (García-Ruiz, 1994), which proposes that dendrites are fingers of infiltrating Mn-rich fluids that solidify by reacting with oxygen in the matrix. If this were the case, further pulses of fluid would not proceed along preexisting dendrites, which have a small porosity, but rather in the porous material between existing dendrites, forming new dendrites. The banding structure is thus further evidence of particle attachment processes, triggered by fluid pulses.

Our model is thus more in line with the diffusion-limited aggregation model of Mn dendrite formation (Chopard et al., 1991), which suggests that they form by aggregation of diffusing particles, although the details of this process and the nature of the particles remain unspecified. Our model also shares features with growth models for gold/electrum dendrites (Schoenly and Saunders, 1993; Saunders et al., 2020), in which dendrites form by the accretion of colloidal particles created deep in hydrothermal systems and carried up to epithermal settings. An alternative mechanism for the growth of gold dendrites, based on ion addition, was proposed by Monecke et al. (2023).

Note that amorphous aggregation dendrites (like those studied here) are morphologically significantly different from crystalline dendrites growing in supercooled melts seen in metallurgy (Trivedi and Kurz, 1994; Haxhimali et al., 2006). The latter are usually needle-like, with a strong dependence on crystal anisotropy and thermal effects. Petrologically, such dendritic crystals often form due to crystallization in rapidly cooled magmas (cf. Welsch et al., 2013; Barbey et al., 2019).

Numerical Modeling of Dendrite Growth

We numerically modeled dendrite formation using the lattice Boltzmann method (Sukop and Thorne, 2010), tracking the diffusing populations of Mn ions and oxygen molecules as well as the reaction between them that led to the formation of Mn-oxide nanoparticles. The nanoparticle population was then tracked, as well as their aggregation on dendrite surfaces (Supplemental Material). As shown in the morphological diagram (Fig. 4B; see also Supplemental Material methods; Fig. S1A), the model gives a variety of structures, depending primarily on the concentrations of the reacting species as well as the magnitude of the surface energy. The morphologies range from highly branched, fractal aggregates with thin trunks to bulkier structures, broadening upward; this is consistent with our natural dendrite forest.

Based on parameters defined by the two-dimensional models, a 3-D model was run. The corresponding phase diagram is shown in Figure S1B. Comparison of the modeled dendrites with the natural structures suggests that Mn and oxygen concentrations should be of the same order during dendrite formation, whereas the surface energy effects are in the intermediate range ($\kappa \sim 4.5$).

The numerical dendrite morphologies are very similar to the natural examples (Fig. 4A, a1–a4; Movie S2). First, the decreasing total dendrite abundance and increasing dendrite width with greater distance from the fracture surface were reproduced by the model, as a result of growth competition between the individual dendrites. Second, the fractal dimension of 2.74 for the model is compatible with 2.7–2.8

in the natural system. Third, the dendrite volume fraction as a function of distance from the fracture in the numerical model is also similar to the natural forest (Fig. S4): There is a pronounced maximum at small distances, corresponding to the forest base and Bi, with volume fractions up to 44%, followed by a plateau corresponding to Bii–iii, with volume fractions of ∼25%; for longer distances from the fracture plane, the dendrite volume fraction sharply decreases.

IMPLICATIONS

Particle attachment processes are increasingly being recognized as a nonclassical but widespread and significant crystallization pathway (Ivanov et al., 2014; De Yoreo et al., 2015). Our work demonstrates that the growth of the 3-D dendrite forest proceeded via particle attachment, and, given the relative simplicity of the system, this constitutes a perfect testing ground to investigate the interplay of diffusion and surface energy effects in the growth dynamics.

Our dendrites are a prime example of chemically driven self-organization, with the system, initially driven out of equilibrium by external fluid pulses, returning to equilibrium by forming Mn-oxide nanoparticles and then aggregating them into dendrites. The efficiency of this process is remarkable, since no Mn remains in the rock matrix. This suggests that particle formation and subsequent attachment to the dendrites could be an effective method for environmental remediation, as conjectured by De Yoreo et al. (2015). In this way, the spontaneous formation of 3-D mineral dendrites can be seen as a “self-purification” of the porous medium, offering the prospect for their use in environmental and groundwater remediation (e.g., Yeritsyan et al., 2013; Cataldo et al., 2021).

The particle attachment mechanism responsible for the growth of our dendrites has similarities with colloidal deposition models for the formation of gold/electrum dendrites (Schoenly and Saunders, 1993; Saunders and Burke, 2017; Saunders 2022). This might lead to a better understanding of the formation mechanism of ultrahigh-grade gold (“bonanza”) veins (McLeish et al, 2021).

Finally, since mineral dendrite growth is sensitive to the volume of infiltrating fluid and Mn ion concentrations, the dendrite structure encodes the hydrogeochemical history of the rock in itself.

ACKNOWLEDGMENTS

This study was funded by the Department of Geology, University of Vienna, and Glock Health, Sciences and Research GmbH (Project ID: FA536901). Piotr Szymczak was funded by the National Science Centre (NCN; Poland) under CEUS-UNISONO grant 2020/02/Y/ST3/00121. E. Matiasek is thanked for X-ray diffraction work.

REFERENCES CITED

Barbey, P., Faure, F., Paquette, J.L., Pistre, K., Delangle, C., and Gremilliet, J.P., 2019, Skeletal quartz and dendritic biotite: Witnesses of primary disequilibrium growth textures in an alkali-feldspar granite: Lithos, v. 348–349, https://doi.org/10.1016/j.lithos.2019.105202.

Cataldo, E., Salvi, L., Paoli, F., Fucile, M., Masciandaro, G., Manzi, D., Masini, C.M., and Mattii, G.B., 2021, Application of zeolites in agriculture and other potential uses: A review: Agronomy (Basel), v. 11, https://doi.org/10.3390/agronomy11081547.

Chopard, B., Herrmann, H.J., and Vicsek, T., 1991, Structure and growth mechanism of mineral dendrites: Nature, v. 353, p. 409–412, https://doi.org/10.1038/353409a0.

De Yoreo, J.J., et al., 2015, Crystallization by particle attachment in synthetic, biogenic, and geologic environments: Science, v. 349, https://doi.org/10.1126/science.aaa6760.

Fowler, A.D., Stanley, H.E., and Daccord, G., 1989, Disequilibrium silicate mineral textures: Fractal and non-fractal features: Nature, v. 341, p. 134–138, https://doi.org/10.1038/341134a0.

García-Ruiz, J.M., Otálora, F., Sanchez-Navas, A., and Higes-Rolando, F.J., 1994, The formation of manganese dendrites as the mineral record of flow structures, *in* Renffel, L.O., ed., Fractals and Dynamic Systems in Geoscience: Berlin, Springer, p. 307–318, https://doi.org/10.1007/978-3-662-07304-9_23.

Haxhimali, T., Karma, A., Gonzales, F., and Rappaz, M., 2006, Orientation selection in dendritic evolution: Nature Materials, v. 5, p. 660–664, https://doi.org/10.1038/nmat1693.

Hochella, M.F., Jr., et al., 2019, Natural, incidental, and engineered nanomaterials and their impacts on the Earth system: Science, v. 363, https://doi.org/10.1126/science.aau8299.

Huang, M., Li, F., Dong, F., Zhang, Y.X., and Zhang, L.L., 2015, MnO_2-based nanostructures for high-performance supercapacitors: Journal of Materials Chemistry A–Materials for Energy and Sustainability, v. 3, p. 21,380–21,423, https://doi.org/10.1039/C5TA05523G.

Ivanov, V.K., Fedorov, P.P., Baranchikov, A.Y., and Osiko, V.V.E., 2014, Oriented attachment of particles: 100 years of investigations of non-classical crystal growth: Russian Chemical Reviews, v. 83, 1204, https://doi.org/10.1070/RCR4453.

Krug, J., 1997, Origins of scale invariance in growth processes: Advances in Physics, v. 46, p. 139–282, https://doi.org/10.1080/00018739700101498.

Li, D., Yang, J., Tang, W., Wu, X., Wei, L., and Chen, Y., 2014, Controlled synthesis of hierarchical MnO_2 microspheres with hollow interiors for the removal of benzene: RSC Advances, v. 4, p. 26,796–26,803, https://doi.org/10.1039/c4ra01146e.

McLeish, D.F., Williams-Jones, A.E., Vasyukova, O.V., Clark, J.R., and Board, W.S., 2021, Colloidal transport and flocculation are the cause of the hyperenrichment of gold in nature: Proceedings of the National Academy of Sciences of the United States of America, v. 118, https://doi.org/10.1073/pnas.2100689118.

Meakin, P., and Deutch, J.M., 1984, Monte Carlo simulation of diffusion controlled colloid growth rates in two and three dimensions: The Journal of Chemical Physics, v. 80, p. 2115–2122, https://doi.org/10.1063/1.446977.

Meakin, P., and Jamtveit, B., 2010, Geological pattern formation by growth and dissolution in aqueous systems: Proceedings of the Royal Society A–Mathematical, Physical and Engineering Sciences, v. 466, p. 659–694, https://doi.org/10.1098/rspa.2009.0189.

Monecke, T., Reynolds, T.J., Taksavasu, T., Tharalson, E.R., Zeeck, L.R., Guzman, M., Gissler, G., and Sherlock, R., 2023, Natural growth of gold dendrites within silica gels: Geology, v. 51, p. 189–192, https://doi.org/10.1130/G48927.1.

Saunders, J.A., 2022, Colloids and nanoparticles: Implications for hydrothermal precious metal ore formation: SEG Discovery, v. 130, p. 15–21, https://doi.org/10.5382/SEGnews.2022-130.fea-01.

Saunders, J.A., and Burke, M., 2017, Formation and aggregation of gold (electrum) nanoparticles in epithermal ores: Minerals (Basel), v. 7, p. 163–174, https://doi.org/10.3390/min7090163.

Saunders, J.A., Burke, M., and Brueseke, M.E., 2020, Scanning-electron-microscope imaging of gold (electrum) nanoparticles in middle Miocene bonanza epithermal ores from northern Nevada, USA: Mineralium Deposita, v. 55, p. 389–398, https://doi.org/10.1007/s00126-019-00935-y.

Schoenly, P.A., and Saunders, J.A., 1993, Natural gold dendrites from hydrothermal Au-Ag deposits—Characteristics and computer simulations: Fractals, v. 1, p. 585–593, https://doi.org/10.1142/S0218348X93000617.

Sukop, M.C., and Thorne, D.T., 2010, Lattice Boltzmann Modelling: Berlin, Springer, 184 p.

Szymczak, P., and Ladd, A.J.C., 2006, A network model of channel competition in fracture dissolution: Geophysical Research Letters, v. 33, L05401, https://doi.org/10.1029/2005GL025334.

Trivedi, R., and Kurz, W., 1994, Dendritic growth: International Materials Reviews, v. 39, p. 49–74, https://doi.org/10.1179/imr.1994.39.2.49.

Tschegg, C., Rice, A.H.N., Grasemann, B., Matiasek, E., Kobulej, P., Dzivák, M., and Berger, T., 2019, Petrogenesis of a large-scale Miocene zeolite tuff in the eastern Slovak Republic: The Nižný Hrabovec open-pit clinoptilolite mine: Economic Geology, v. 114, p. 1177–1194, https://doi.org/10.5382/econgeo.4679.

Tschegg, C., Hou, Z., Rice, A.H.N., Fendrych, J., Matiasek, E., Berger, T., and Grasemann, B., 2020, Fault zone structures and strain localization in clinoptilolite-tuff (Nižný Hrabovec, Slovak Republic): Journal of Structural Geology, v. 138, https://doi.org/10.1016/j.jsg.2020.104090.

Van Straaten, L.M.J.U., 1978, Dendrites: Journal of the Geological Society, v. 135, p. 137–151, https://doi.org/10.1144/gsjgs.135.1.0137.

Voss, R.F., 1984, Multiparticle diffusive fractal aggregation: Physical Review B, v. 30, p. 334–337, https://doi.org/10.1103/PhysRevB.30.334.

Welsch, B., Faure, F., Famin, V., Baronnet, A., and Bachèlery, P., 2013, Dendritic crystallization: A single process for all the textures of olivine in basalts?: Journal of Petrology, v. 54, p. 539–574, https://doi.org/10.1093/petrology/egs077.

Yeritsyan, H., Sahakyan, A., Harutyunyan, V., Nikoghosyan, S., Hakhverdyan, E., Grigoryan, N., Hovhannisyan, A., Atoyan, V., Keheyan, Y., and Rhodes, C., 2013, Radiation-modified natural zeolites for cleaning liquid nuclear waste (irradiation against radioactivity): Scientific Reports, v. 3, https://doi.org/10.1038/srep02900.

Printed in USA